Journal of Rock Mechanics and Geotechnical Engineering 18 (2026) 3675–3687

Contents lists available at ScienceDirect

Journal of Rock Mechanics and Geotechnical Engineering

journal homepage: www.jrmge.cn

Full Length Article

A physics-based probabilistic method for assessment of landslide-induced wave run-up hazards

Ningjie Li, Xinli Hu *, Jian Wang, Junxiang Huang, Hongchao Zheng, Wei Li

Faculty of Engineering, China University of Geosciences, Wuhan, 430074, China

ARTICLE INFO

Article history:
Received 31 January 2025
Received in revised form
2 June 2025
Accepted 10 June 2025
Available online 20 August 2025

Keywords:
Landslide-induced wave run-up (LIWR)
Numerical simulation
Adaptive metamodel
Probability density evolution method (PDEM)
Hazard zoning

ABSTRACT

Traditional deterministic numerical simulation often has a poor prediction performance for landslide-induced wave run-up (LIWR) hazards, as it neglects the effects of uncertainty. The limitation for efficiently quantifying the uncertainties in primary parameters remains largely unsolved. In this study, we propose a probabilistic evaluation method, integrating the adaptive Kriging (AK) metamodel method and probability density evolution method (PDEM) based on generalized F-discrepancy. A Taylor expansion-based adaptive design strategy is applied to construct the global AK model over representative points generated by generalized F-discrepancy, thereby approximating the numerical physical response (i.e., maximum LIWR). Using these approximate responses, the PDEM is used to compute the exceedance probabilities that LIWR heights exceed elements at risk based on a construction of virtual time, and then a probabilistic criterion is introduced to classify hazard zones. The proposed method is demonstrated via two examples: Example I, which possesses risk element (building), and Example II with water-level variations. The results indicate that the proposed method has an acceptable performance (showing a 1.7 % difference in exceedance probability compared to Monte Carlo simulation with 50,000 samples) with low computation cost (requiring 284 deterministic analyses). For two specific scenarios in this study, the wave induced by the landslide exhibits a solitary-like leading wave. The proposed probabilistic method provides promising prospects for quantifying LIWR uncertainties, and is helpful for direct, efficient, and low-cost quantification assessment of cascading hazards.
© 2026 Institute of Rock and Soil Mechanics, Chinese Academy of Sciences. Published by Elsevier B.V. This is an open access article under the CC BY-NC-ND license (http://creativecommons.org/licenses/by-nc-nd/4.0/).

1. Introduction

The increase in the number of artificial reservoirs promotes the effect of slope erosion and river scouring (Wiegel et al., 1970; Panizzo et al., 2005a), thereby accelerating the occurrence of geological hazards, such as landslides (Yin et al., 2016; Liu et al., 2024), and rock avalanches (Zhang et al., 2024). Regardless of their evolution mechanisms, the resulting cascading hazards typically pose a potential threat to residents and communities along reservoir banks, including inundation by impulse waves (Huang and Hu, 2023; Huang and Dong, 2024; Ma et al., 2024; Svennevig et al., 2024). Wave run-up, a key disaster phenomenon of land inundation, is thus of importance for accurately predicting the fluid flow involved in these chain reactions.

In the past decades, landslide-generated wave run-up has usually typically been reproduced through prototype-specific physical model trials (Wiegel, 1955; Kamphuis and Bowering, 1970; Wiegel et al., 1970; Enet et al., 2003; Walder et al., 2003; Fritz et al., 2004; Panizzo et al., 2005b; Di Risio et al., 2009) and numerical studies (Watts et al., 2003; Bellotti et al., 2008; Cecioni et al., 2011; Yavari-Ramshe and Ataie-Ashtiani, 2016; Grilli et al., 2017; Whittaker et al., 2017; Ruffini et al., 2019; Gibbons et al., 2020). In contrast, the latter approach offers high efficiency and low cost, while capturing the physical evolution of wave generation and inundation (Latifah et al., 2024; Wu et al., 2024). Several scholars have addressed the fluid-solid coupling problem by approximating both the sliding mass and the water as distinct fluid phases. This strategy enables practical numerical simulations of sliding and wave-generation processes by combining: Eulerian or Lagrangian frameworks (Løvholt et al., 2005; Kim et al., 2019) to describe fluid/solid kinematics, structured or unstructured grids (Lynett and Liu, 2005; Si et al., 2018) for spatial discretization, and numerical methods such as finite difference method (Zhao et al., 2016), finite element method (Mulligan et al., 2020), or finite

* Corresponding author.
E-mail address: huxinli@cug.edu.cn (X. Hu).
Peer review under responsibility of Institute of Rock and Soil Mechanics, Chinese Academy of Sciences.

https://doi.org/10.1016/j.jrmge.2025.06.018
1674-7755/© 2026 Institute of Rock and Soil Mechanics, Chinese Academy of Sciences. Published by Elsevier B.V. This is an open access article under the CC BY-NC-ND license (http://creativecommons.org/licenses/by-nc-nd/4.0/).

volume method (Franco et al., 2021) to solve governing equations. Although these computational approaches can provide robust data for quantitative risk assessment, their principal limitation lies in the challenge of accurately determining the relevant model parameters in practical applications. This difficulty amplifies parameter uncertainty and compromises predictive accuracy.

Currently, information on model parameters is primarily obtained through laboratory experiments (Li et al., 2024b) and simulation-based trial-and-error methods, which involve parameter back-analysis (Li et al., 2024a) performed through post-hoc numerical simulation. Although the combined use of these two approaches can yield relevant parameter ranges, it does not necessarily identify the most suitable values for forward prediction. Because deterministic models rely on fixed values for each input parameter (Zhang et al., 2023; Jiang et al., 2024), they produce only a single target response (e.g., landslide-induced wave run-up (LIWR) height). In reality, some primary model parameters are not precisely known and involve varying degrees of uncertainty. Therefore, deterministic models are typically coupled with reliability analysis techniques to quantify the uncertainty of related model parameters, thereby improving the performance of risk assessment (Iorio et al., 2021; Cecioni et al., 2023).

Geotechnical reliability analysis related to reservoir landslides has attracted increasing attention in engineering practice (Liao et al., 2024). Most of the literature focuses on slope stability and landslide run-out analysis (Wang et al., 2024; Wu et al., 2023), while the research on the probabilistic assessment of landslide-induced waves is rarely reported (Grilli et al., 2009; Behrens et al., 2021). These methods can generally be categorized into three types. (1) Approximation methods including the first-/second-order reliability method (FORM/SORM) (Yang et al., 2024), which rely on related Taylor expansions of the performance function (PF) around the most probable point (MPP). These methods can be hampered by several MPPs and the nonlinearity of the PF. (2) Sampling approaches, such as Monte Carlo simulation (MCS) (Wang et al., 2023; Tian et al., 2024a,b) and its derivatives (e.g. importance sampling (Engelund and Rackwitz, 1993), line sampling (Pradlwarter et al., 2007)), which are robust and straightforward but become computationally intensive when time-consuming deterministic analyses. (3) Surrogate computation (also called metamodels) approaches, which employ constructed surrogate models, such as Kriging (Yang et al., 2022), radial basis functions (Javdanian and Pradhan, 2019), support vector machines (Yang et al., 2023), and artificial neural networks (Li et al., 2021), to approximate complex target responses and thereby reduce the computation cost. However, the performance of these approaches largely depends on the chosen metamodel type and sampling strategy. In the context of probabilistic tsunami hazard analysis (PTHA), Alhamid et al. (2022) used radial-basis-function-based surrogates in combination with quasi-MCS to construct tsunami hazard curves. Similarly, Tozato et al. (2023) applied genetic algorithms and surrogate models to estimate hazard indices.

Additionally, Li et al. (2004) introduced the probability density evolution method (PDEM), which captures the instantaneous probability density function (PDF) of nonlinear stochastic structural responses based on the probabilistic density conservation theory. By leveraging the concept of the equivalent extreme value (EEV) event (Chen and Li, 2007), PDEM enables the evaluation of first-passage probabilities. The method involves partitioning the probability space, and advanced sampling strategies have been developed for this purpose, such as the tangent sphere method (Chen and Li, 2008) and the GF-discrepancy approach (Chen et al., 2016). Among these, GF-discrepancy sampling technology has garnered considerable attention for its ability to produce uniformly distributed point sets. Although GF-discrepancy-based PDEM typically meets the requirements of numerical analyses with relatively low computational loads (e.g. slope stability), it remains challenging for highly nonlinear fluid dynamics simulations. To this end, a metamodeling strategy is adopted, partitioning the model into local components—used to approximate responses within specific regions—and a global component. Because the GF-discrepancy method generates representative points across the entire multivariate parameter domain, PDEM usually requires a global surrogate model to approximate the responses at these representative points.

Quantifying uncertainties is a complex aspect for the LIWR hazard with cascading effects. To this end, the primary purposes of this study are as follows: (1) Propose a method to quantify uncertainties of primary model parameters in the numerical model; (2) Reduce the computational cost of probabilistic analysis compared to the traditional MCS; and (3) Introduce the probabilistic criterion to optimize the traditional deterministic evaluation.

Generally, this study proposes an efficient reliability method, AK-PDEM, which combines the adaptive global Kriging (AK) metamodel and PDEM to evaluate exceedance probabilities and hazard zones for LIWR. A Taylor expansion-based adaptive design strategy is employed to construct a global surrogate model that approximates the relationship between LIWR responses and the random variables characterizing the landslide-wave probability analysis. Section 2 introduces the methodologies, and Section 3 details the implementation workflow. In Section 4, the feasibility and effectiveness of AK-PDEM are demonstrated through two illustrative scenario-based examples.

2. Methodology

In this section, we first describe the fluid dynamics simulation, and then introduce the methods for the AK metamodel and TEAD strategy. Additionally, the PDEM theories for computing the probability distribution of wave run-up caused by landslides are presented. Finally, the implementation of AK-PDEM is elucidated.

2.1. Numerical simulation of fluid dynamics

In this study, granular media model in Flow3D is applied to simulate the physical process of landslide impacting the water body, which serves as the basis for capturing run-up heights through the renormalized group (RNG) model mimicking flow with a high strain rate and large streamline curvature (Flow Science Inc, 2020; Yi et al., 2023). The RNG model has more accuracy in low-intensity turbulence flows compared to the traditional k-ε model, aiding in capturing wave characteristics (Montagna et al., 2011). The equations of fluid motion are as follows:

$$\frac{\partial \varepsilon_T}{\partial t}+\frac{1}{V_F}\left(uA_x\frac{\partial \varepsilon_T}{\partial x}+vA_y\frac{\partial \varepsilon_T}{\partial y}+wA_z\frac{\partial \varepsilon_T}{\partial z}\right)=\frac{\mathrm{CDIS}_1\cdot\varepsilon_T}{k_T}\left(P_T+\mathrm{CDIS}_3\cdot G_T\right)+\mathrm{Diff}_\varepsilon-\mathrm{CDIS}_2\cdot\frac{\varepsilon_T^2}{k_T} \tag{1}$$

$$\frac{\partial k_T}{\partial t}+\frac{1}{V_F}\left(uA_x\frac{\partial k_T}{\partial x}+vA_y\frac{\partial k_T}{\partial y}+wA_z\frac{\partial k_T}{\partial z}\right)=P_T+G_T+\mathrm{Diff}_{k_T}-\varepsilon_T \tag{2}$$

where u, v, and w, are the depth-averaged values of x y, and z, respectively; ε_T, k_T, P_T, and G_T denote the rate of turbulent energy dissipation, the turbulent kinetic energy, the turbulent kinetic energy production, and the buoyancy production, respectively; A_x, A_y, and A_z represent the effective flow areas in their respective coordinate directions x, y, and z, respectively; $\mathrm{Diff}_\varepsilon$ and Diff_{k_T} denote diffusion terms; CDIS_1 and CDIS_3 mean user-configurable dimensionless coefficients with default values of 1.42 and 0.2, respectively, while CDIS_2 is functionally dependent on the k_T and P_T (Flow Science Inc, 2020; Chen et al., 2023).

The granular media model is used to reproduce the solid particles and fluids, and its state is a single-phase continuous fluid similar to a non-Newtonian fluid (Hirt, 2010). This mixture fluid model is defined as an incompressible fluid with shear stresses (Chen et al., 2023). Therefore, Franco et al. (2021) and Li et al. (2024a) pointed out that effective dynamic viscosity τ_{eff} is essential for landslide flow, determining the movement pattern and kinetic energy of the landslide entering water, further influencing near-field wave generation. Once the maximum wave height changes, the far-field wave run-up will also be affected. The effective dynamic viscosity τ_{eff} is expressed by Mih's equation in Flow3D (Franco et al., 2021):

$$\tau_{\mathrm{eff}}=7.8\tau_w\left(\frac{\lambda^2}{1+\lambda}\right)+0.066\rho_g(\lambda d)^2|e_{ij}| \tag{3}$$

where τ_w and e_{ij} are the fluid viscosity and the strain rate, respectively; λ is the maximum volume ratio between grain diameter d (m) and grain gap S (m); and ρ_g (kg/m^3) is the grain density. In light of Eq. (3) and found by Li et al. (2024a), d and ρ_g are the primary parameters for LIWR. Additionally, based on sensitivity analysis, Franco et al. (2021) pointed out that the surface roughness parameter (R_r), used to consider the attenuation of geomorphic differences, is also important for tsunami run-up. Flow3D implements R_r, characterized by equivalent grain height, which can be set for each model domain. This enables hydrodynamic simulations to account for surface properties (e.g. vegetation, grains, topographic variations) beyond the geometric resolution of imported STL files (Franco et al., 2021). Consequently, the three factors, determining the heights of wave run-up, are herein defined as the primary random variables in the landslide-wave probabilistic analysis. In order to emphasize the influence of the determined model parameters on wave run-up, we performed a sensitivity analysis in the Discussion section.

2.2. Metamodel and design strategy

2.2.1. Kriging model

Kriging surrogate models can approximate the responses of numerical simulation, reducing the computation cost. In other words, the Kriging model is used to map the nonlinear relationship between random variables $\boldsymbol{\theta}$ and the simulated wave run-up heights $H(\boldsymbol{\theta})$:

$$H(\boldsymbol{\theta})=\mathrm{Kriging}(\boldsymbol{\theta}):H_s\approx H_k=\boldsymbol{\beta}^{\mathrm{T}}f(\boldsymbol{\theta})+\sigma_g^2Z(\boldsymbol{\theta}) \tag{4}$$

where H_s and H_k are the actual physical response and response computed by the Kriging model, respectively; $\boldsymbol{\beta}^Tf(\boldsymbol{\theta})$ is the trend term; $f(\boldsymbol{\theta})=f_1(\boldsymbol{\theta}),\ldots,f_p(\boldsymbol{\theta})$ and p present the basis function vector and its number; $\boldsymbol{\beta}=\left[\beta_1,\ldots,\beta_p\right]$ denotes the unknown coefficients. σ_g^2 means the variance of the Gaussian stochastic process; and $Z(\boldsymbol{\theta})$ means the standard Gaussian stochastic process with a mean of 0 and variance of 1. In this study, we employ the Ordinary Kriging model with the kernel function.

2.2.2. Taylor expansion-based adaptive design strategy

In this study, we used the Taylor expansion-based adaptive design (TEAD) to update the approximate performance of the surrogate model. The remainder of the first-order Taylor expansion $R_{\mathrm{rem}}(\boldsymbol{\theta})$ and the minimum Euclidean distance $E_{\min}$ are used to explore local and global exploitations, which are detailed as follows (Mo et al., 2017):

$$R_{\mathrm{rem}}(\boldsymbol{\theta})=\left|\widehat{M}(\boldsymbol{\theta})-\left[\widehat{M}_{\mathrm{T}}(\boldsymbol{\theta}_{\mathrm{near}})+\nabla\widehat{M}(\boldsymbol{\theta}_{\mathrm{near}})^{\mathrm{T}}(\boldsymbol{\theta}-\boldsymbol{\theta}_{\mathrm{near}})\right]\right| \tag{5}$$

$$E_{\min}=\min_{\boldsymbol{\theta}^{(j)}\in\boldsymbol{\Theta}}\parallel\boldsymbol{\theta}-\boldsymbol{\theta}^{(j)}\parallel \tag{6}$$

where $\boldsymbol{\theta}^{(j)}$ is the j-th training sample in sample pool $\boldsymbol{\theta}$; $\boldsymbol{\theta}_{\mathrm{near}}\in\boldsymbol{\Theta}$ denotes the nearest training sample to the candidate $\boldsymbol{\theta}$, and $\nabla\widehat{M}(\boldsymbol{\theta}_{\mathrm{near}})$ presents the first-order gradient of $\widehat{M}(\boldsymbol{\theta})$ at $\boldsymbol{\theta}_{\mathrm{near}}$ via the difference method to solve. Therefore, the TEAD can be expressed as

$$\mathrm{TEAD}(\boldsymbol{\theta})=\omega(\boldsymbol{\theta})\frac{R_{\mathrm{rem}}(\boldsymbol{\theta})}{\max\limits_{\boldsymbol{\theta}\in\boldsymbol{\Theta}_{\mathrm{rep}}}R_{\mathrm{rem}}(\boldsymbol{\theta})}+\frac{E_{\min}(\boldsymbol{\theta})}{\max\limits_{\boldsymbol{\theta}\in\boldsymbol{\Theta}_{\mathrm{rep}}}E_{\min}(\boldsymbol{\theta})} \tag{7}$$

where $\omega(\boldsymbol{\theta})=1-E_{\min}(\boldsymbol{\theta})/E_{\max}(\boldsymbol{\theta})$ is the weight function, and $E_{\max}(\boldsymbol{\theta})$ is the maximum distance of two samples. The new sample is obtained from the representative point pool constructed by GF-discrepancy, aiming to update the approximate function of the AK model in this sample pool. The new sample selection can be expressed as

$$\boldsymbol{\theta}_{\mathrm{new}}=\arg\max_{\boldsymbol{\theta}\in\boldsymbol{\Theta}_{\mathrm{rep}}}\mathrm{TEAD}(\boldsymbol{\theta}) \tag{8}$$

Since the actual physical response $\boldsymbol{H}_{\mathrm{rep}}=\left\{H_{\mathrm{rep}}^{(1)},\ldots,H_{\mathrm{rep}}^{(N_{\mathrm{rep}})}\right\}$ of the representative point computed by numerical simulation is unknown, an optimized termination criterion is proposed:

$$\mathrm{NRMSE}_{\mathrm{new}}=\frac{\sqrt{(H_{\mathrm{new}}-\widehat{M}(\boldsymbol{\theta}_{\mathrm{new}}))^2}}{\max\limits_{1\le i\le N}H_{\mathrm{rep}}^{(i)}-\min\limits_{1\le i\le N}H_{\mathrm{rep}}^{(i)}}<\varepsilon_{\mathrm{NRMSE}} \tag{9}$$

A convergence $\varepsilon_{\mathrm{NRMSE}}$, where Eq. (9) is satisfied in five consecutive iteration steps, is set to ensure the robustness of the surrogate model.

2.3. PDEM

For the time-independent problem in this study, we utilized PDEM to compute the probability distribution of wave run-up height, through a construction of the 0–1 virtual time (Chen and Li, 2008). Consequently, integrating the response of the AK model $\widehat{M}(\boldsymbol{\theta})$, LIWR heights $H(t)$ at this virtual time can be expressed as

$$H(t)=\widehat{M}(\boldsymbol{\theta},t)=\widehat{M}(\boldsymbol{\theta})t \tag{10}$$

In light of probability conservation theory, a stochastic condition ($H(t)$, $\boldsymbol{\theta}$) is constructed for all random variables, and the generalized density evolution equation is derived as

$$\frac{\partial p_{H\boldsymbol{\theta}}(h,\boldsymbol{\theta},t)}{\partial t}+\dot{\hat{M}}(\boldsymbol{\theta},t)\frac{\partial p_{H\boldsymbol{\theta}}(h,\boldsymbol{\theta},t)}{\partial h}=0 \tag{11}$$

where $p_{H\boldsymbol{\theta}}(h,\boldsymbol{\theta},t)$ is joint PDFs of $(H(t),\boldsymbol{\theta})$; $\dot{\hat{M}}(\boldsymbol{\theta},t)$ is the evolution rate of $\hat{M}(\boldsymbol{\theta})$, and its initial condition:

$$p_{H\boldsymbol{\theta}}(h,\boldsymbol{\theta},t)|_{t=0}=\delta(h-h_0)p_{\boldsymbol{\theta}}(\boldsymbol{\theta}) \tag{12}$$

where $p_{\boldsymbol{\theta}}(\boldsymbol{\theta})$ presents PDFs of $\boldsymbol{\theta}$, $\delta(\cdot)$ is the Dirac function, and h_0 is the initial value.

Firstly, for solving Eq. (11) in previous literature (Chen et al., 2016), a discrete set of representative points $\boldsymbol{\theta}_{\text{rps}}$ (rps = 1, 2, ⋯, N, where N is the total number of representative points) is selected in the distribution domain of $\boldsymbol{\theta}$ based on the GF-discrepancy (Chen et al., 2016). The assigned probability P_{rep} for each representative point is then obtained by integrating PDFs of $\boldsymbol{\theta}$ over the corresponding Voronoi cell. Consequently, Eq. (10) can be expressed in discrete form as follows:

$$\frac{\partial p_{H\boldsymbol{\theta}}(h,\boldsymbol{\theta}_{\text{rps}},t)}{\partial t}+\dot{\hat{M}}(\boldsymbol{\theta},t)\frac{\partial p_{H\boldsymbol{\theta}}(h,\boldsymbol{\theta}_{\text{rps}},t)}{\partial h}=0 \tag{13}$$

where the rps = 1, 2, …, N, N is typically 1000; Eq. (12) can be derived as $p_{H\boldsymbol{\theta}}(h,\boldsymbol{\theta}_{\text{rps}},t)|_{t=0}=\delta(h-h_0)P_{\text{rps}}$.

Secondly, the representative point $\boldsymbol{\theta}_{\text{rps}}$ is substituted into the surrogate model to provide the wave run-up heights $\dot{\hat{M}}(\boldsymbol{\theta},t)$ and then obtain the related derivative $\dot{\hat{M}}(\boldsymbol{\theta},t)$. Thirdly, Eq. (13) is solved using the finite difference method and then the discretized joint PDFs $p_{H\boldsymbol{\theta}}(h,\boldsymbol{\theta}_{\text{rps}},t)$ are provided. Finally, PDFs $p_H(y,t)$ of the LIWR heights $H(t)$ are provided through the sum of $p_{H\boldsymbol{\theta}}(h,\boldsymbol{\theta}_{\text{rps}},t)$:

$$p_H(h,t)=\sum_{\text{rps}=1}^{N}p_{H\boldsymbol{\theta}}(h,\boldsymbol{\theta}_{rps},t) \tag{14}$$

When $t=1$, the PDF of the response of the surrogate model is defined as the PDF of $\hat{M}(\boldsymbol{\theta})$ because $H(t)=\hat{M}(\boldsymbol{\theta})$ in Eq. (10) at $t=1$. In other words, for the time-independent problem, the PDF of LIWR can be obtained by using the PDEM and extracting the PDF of $t=1$.

In order to calculate the exceedance probability and hazard zoning, the performance function is constructed as follows for the element at risk:

$$f_i(\boldsymbol{\theta})=H_{\text{thr}}-H(\boldsymbol{\theta}) \tag{15}$$

where H_{thr} is the given threshold of wave height or run-up height. The probability that the wave run-up height exceeds the given threshold $f_i(\boldsymbol{\theta})\le 0$ is treated as the exceedance probability (P_e), which can be expressed as

$$P_e=P[f_i(\boldsymbol{\theta})\le 0]=\int_{f_i(\boldsymbol{\theta})\le 0}f_{\boldsymbol{\theta}}(\boldsymbol{\theta})\mathrm{d}\boldsymbol{\theta} \tag{16}$$

where $f_{\boldsymbol{\theta}}(\boldsymbol{\theta})$ is the PDF of $\boldsymbol{\theta}$. The P_e can be obtained by using AK-PDEM and Eq. (16).

3. Implementation workflow

The AK-PDEM is composed of three parts (Fig. 1): numerical modeling and preparation (Steps 1–4), adaptive metamodel construction (Steps 5–10), and PDEM (Steps 11–14), which are as follows:

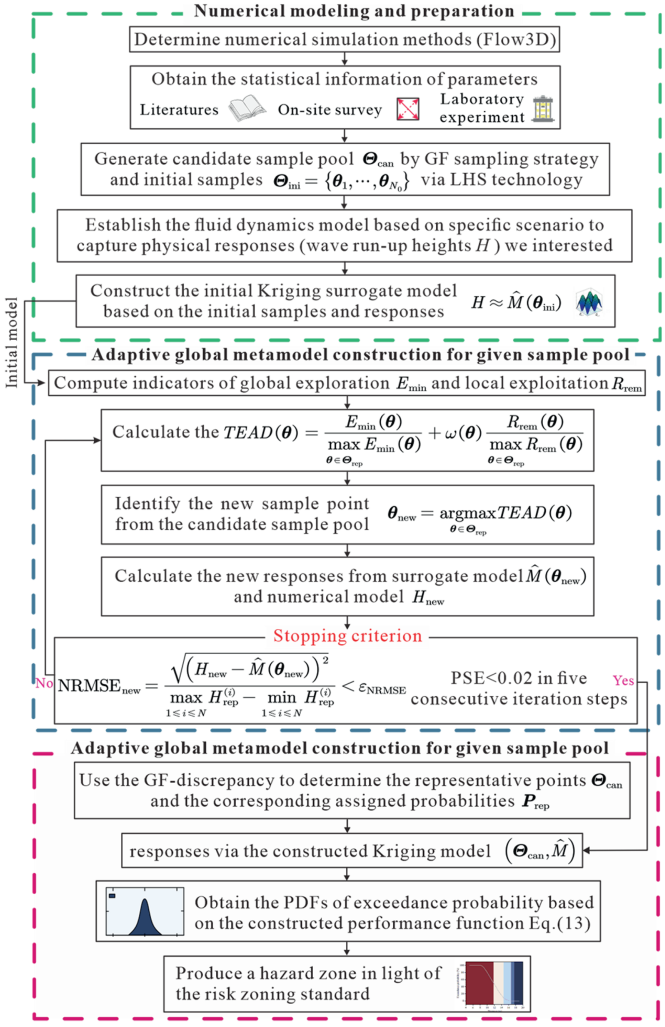

Fig. 1. Flowchart of the AK-PDEM method, including three parts: numerical modeling and preparation (green line), adaptive metamodel construction (blue line), and exceedance probability and hazard zone (red line).

(1) Step 1: Flow3D, which is widely used to reproduce the LIWR, is herein used to capture the wave properties (i.e. wave run-up height).
(2) Step 2: The statistical information of primary parameters determined in Section 2.1 is obtained via the literature, on-site survey, and laboratory experiment.
(3) Step 3: According to the statistical information, the candidate sample pool $\boldsymbol{\Theta}_{\text{can}}$ is constructed by GF-discrepancy technology, and the initial samples $\boldsymbol{\Theta}_{\text{ini}}=\{\theta_1,\ldots,\theta_{N_0}\}$ are generated by Latin hypercube sampling (LHS) technology.
(4) Step 4: The fluid dynamics model for the specific scenario is constructed to capture the physical responses.
(5) Step 5: The initial samples are input in Step 4 to obtain the initial responses, and thus both are used to construct the initial Kriging model.
(6) Steps 6–8: Based on the initial Kriging model, the indicator of global $E_{\min}$ and local E_{rem} exploitations is computed, and then the TEAD($\boldsymbol{\theta}$) in Eq. (7) is calculated. Afterward, according to Eq. (8), the new sample is selected from the candidate sample pool to update the current Kriging surrogate model.
(7) Steps 9 and 10: The new response $\hat{M}(\boldsymbol{\theta}_{\text{new}})$ and simulation H_{new} are computed by the current Kriging surrogate model

and numerical model. Afterward, these results are substituted into Eq. (9) to determine whether they meet the stopping criterion. If yes, the construction of the Kriging surrogate model is finished; if no, it will return to Step 7 for updating the surrogate model continuously.

(8) Step 11: The representative points $\boldsymbol{\Theta}_{\text{can}}$ are generated in Step 3, while the corresponding assigned probabilities $\boldsymbol{P}_{\text{rep}}$ are obtained by the GF-discrepancy.

(9) Steps 12–14: In light of the constructed AK surrogate model in Step 10, responses of all representative points are provided, which are used as basic to compute PDFs of run-up height using the PDEM, and then the exceedance probabilities are calculated via Eq. (16). Finally, a hazard zone is provided based on the given risk standard.

4. Illustrative scenario-based examples

4.1. Example I: landslide-generated wave run-up with building

4.1.1. Three mathematical function tests

Three two-dimensional (2D) mathematical functions are employed to demonstrate the performance of AK with TEAD (Fig. 2), and their expressions are presented in Appendix A; (I) Anisotropy and (II) droplet functions have extreme and relative smooth variations in the domain; (III) Peaks function possesses multimodal whereas the rest of the domain remains unchanged. For simplicity, the variables of these functions are assumed to allow uniform distribution. One thousand representative points are generated by GF-discrepancy, and 20 initial sample points are provided by LHS technology. Moreover, the termination criterion of NRMSE is set as 10^{-2}. In general, predictions of the Kriging models are globally consistent with true values.

4.1.2. Background of example I

The Wangjiashan landslide is located approximately 80 km upstream of the Baihetan hydropower dam site, in WJS village, Nagu town, Huize County, Yunnan Province, China (Fig. 3a and b). Wangjiashan landslide in the Baihetan hydropower station is primarily composed of the Quaternary colluvial deposit and Quaternary landslide deposit, with mixed soil and silty gravels (Yi et al., 2022; Chen et al., 2023). This composition satisfies the requirements for applying the granular media model in Flow3D (Franco et al., 2021). The Xiangbiling resettlement area, located approximately 1.3 km from the landslide (Fig. 3c), faces potential threats from impulse waves triggered by the landslide.

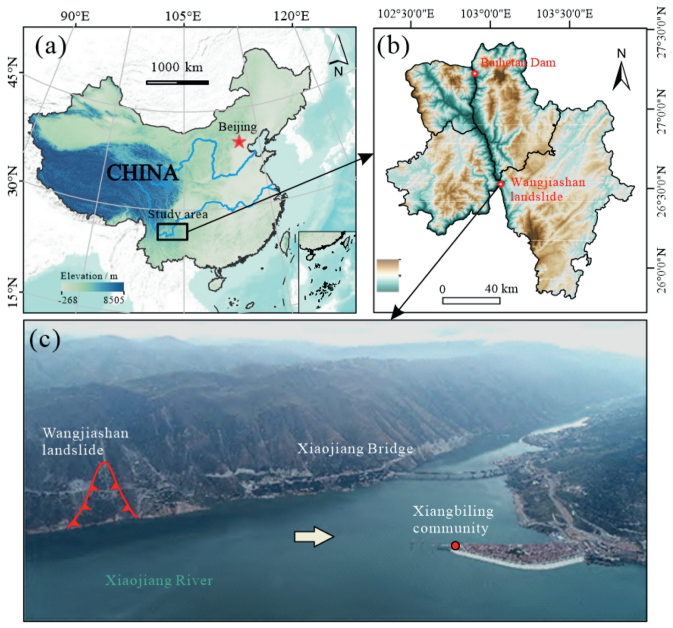

Fig. 3. (a, b) Location of the Wangjiashan landslide; (c) The aerial photomosaic of Wangjiashan landslide and Xiangbiling community, located approximately 1.3 km away.

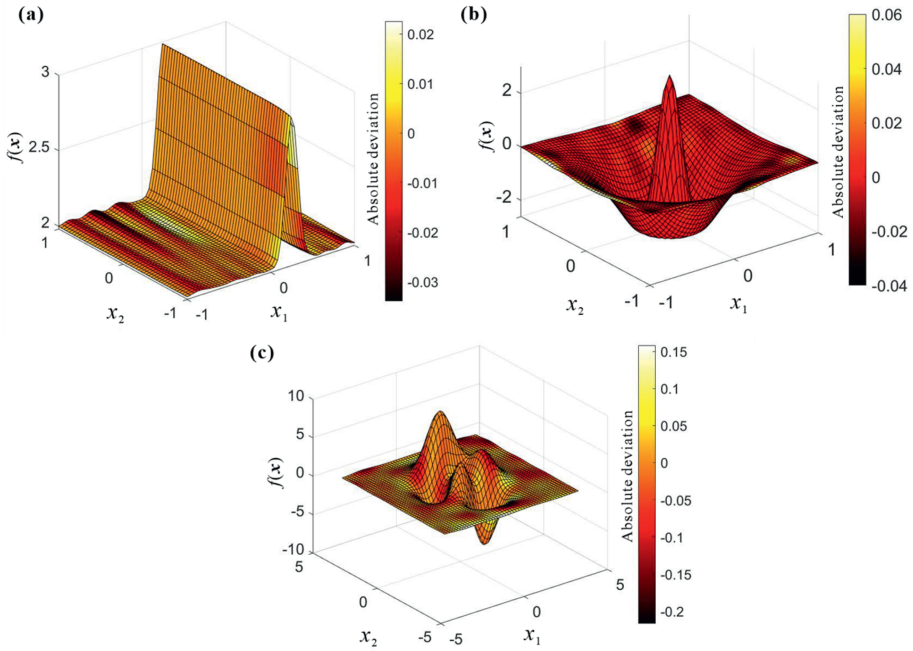

Fig. 2. Performance of the AK model for three 2D mathematical functions: (a) Anisotropy function, (b) Droplet function, and (c) Peaks function.

4.1.3. Deterministic analysis

Based on the background of Example I, we construct a specific ideal-scenario model: LIWR, focusing on the wave height in front of the building. A 2D numerical model has a spatial extent of 1600 m × 250 m in the *X*-*Y* direction (Fig. 4). Although the numerical model is defined as a 2D model, it has a certain thickness. In this study, the thickness of the model is set to 50 m. An orthogonal grid featuring a uniform cell size of 7 m is used, leading to a grid resolution of 51,480. Wall boundaries are set at the top and bottom of the *X*-direction and the bottom of the *Y*-direction (Fig. 4). The standard atmospheric pressure boundary is set at the top of the *Y*-direction. To mitigate wave reflections in the 2D domain, symmetric wave absorbers are placed along the thickness, with the damping coefficient gradually increasing from zero to four (Chen et al., 2024). Under a gravitational acceleration of 9.81 m/s^2, the sliding mass starts from rest and impacts the water. The simulation runs for a duration of 100 s. Probe points, located 65 m from the shore, record the maximum inundation height.

In this section, we focus on exploring the characteristics of tsunami generation, propagation, and maximum wave inundation, which provide the basis for the AK-PDEM. We use two threshold sets of landslide parameters (min: d = 0.01 m, ρ_g = 2150 kg/m^3, R_r = 1 m; max: d = 1 m, ρ_g = 2650 kg/m^3, R_r = 4 m) to simulate physical processes of LIWR. Two simulations are shown in the form of the time sequence in Fig. 5, showing wave generation (t = 10 s), propagation (t = 10–30/50 s), inundation (t = 30/50–70 s), and reflection (t = 100 s). The landslide impact and wave generation are depicted in Fig. 5a and f. For higher basal-slip velocities, landslide flow becomes directed down-slope rather than across the water surface (Fig. 5a). The landslide deposition leads to a flowing basal layer whose velocity decreases because the shear strength of the two-phase and the friction develop both at the flow surface and riverbed. A basal layer is thinner and propagates farther for the minimal landslide parameters. The water body, occupied by the landslide mass, is pushed to develop a solitary-like leading wave, transferring the kinetic energy of the landslide into the wave impulse energy. Afterward, the propagated wave reaches the opposing bank and interacts with the slope to change the direction of wave movement, thus forming a run-up phenomenon on the bank for two simulations (Fig. 5c and i). Wave arrows occur in an aggregation phenomenon at the opposing bank (t = 50 and 70 s), and then the main wave direction changes toward the reflection direction. These observations underscore that the maximum run-up height is possibly affected by the leading wave characterizing the solitary waveform.

4.1.4. Reliability assessment of landslide-induced tsunami

Characterizing random variables is crucial for probabilistic wave hazard zoning because it provides basic input information and significantly affects prediction accuracy. However, due to limited data sources in this study, an idealized distribution of information has been adopted. To this end, improving the reliability and adequacy of data is an important basis for forward prediction. Firstly, when a landslide occurs in a reservoir area, extensive field and laboratory experiments should be conducted promptly to obtain information on essential geotechnical parameters. These parameters can then be categorized by landslide type, facilitating the creation of a regional database focused on reservoir areas. Second, parameter back analysis can be performed using fluid dynamics simulation, and the resulting wave data can be statistically evaluated to guide similar future cases. Finally, due to the suddenness of landslides, it is difficult to achieve the two mentioned points. A Bayesian-based parameter probability back analysis is simulationally performed, and the posterior probability distribution of the calibrating parameter can be directly used for the prediction of landslide-induced waves in the same basin (Li et al., 2024b; Tian et al., 2024a,b).

In Section 2.1, the grain diameter d, density ρ_g, and surface roughness R_r are the primary parameters for LIWR, which are treated as random variables, as they determine the magnitude of wave run-up heights. Their probability distributions are determined based on certain values in numerical simulation and field survey/experiment for this study region, with further details provided in Table 1 (Huang et al., 2017; Kim et al., 2020; Franco et al., 2021; Sabeti and Heidarzadeh, 2022; Chen et al., 2023; Long et al., 2024; Shi et al., 2024; Wu et al., 2024). Specifically, the grain diameter d of 0.01–1 m and grain density ρ_g of 2150–2650 kg/m^3 follow the normal distribution with the 4-sigma rule covering approximately 99 % range. These two ranges are used to characterize a mixture of displaced rock blocks, gravel, silt, and loose soil (Yi et al., 2022). The d and ρ_g are therefore assumed to be a mean of 0.505 m with a standard deviation of 0.124 m and a mean of 2400 kg/m^3 with a standard deviation of 62.5 kg/m^3, respectively. In terms of the surface roughness parameter R_r, it is assumed that a uniform distribution within 1–4 m refers to the suggestion of Franco et al. (2021). This range is used to characterize surface properties (e.g. vegetation, grains, topographic variations) beyond the geometric resolution of imported STL files. Notably, these three parameters are statistically regarded as independent of one another.

The computational cost in the PDEM-based probabilistic assessment predominantly depends on the deterministic fluid dynamics analysis obtaining the maximum wave run-up height. In light of Section 2.3, 1000 representative points are used to compute PDFs, necessitating 1000 corresponding physical responses. To reduce computational overhead, the AK surrogate model with the TEAD strategy is constructed to approximate these 1000 responses. Firstly, the 1000 representative points serve as the candidate sample pool (RE$_v$). According to the three parameters recognized in Section 2.1, 30 initial samples, generated using the LHS method and their physical responses, are used to construct the initial Kriging surrogate model. Afterward, this model is iteratively updated using the TEAD strategy based on new samples from the representative points and corresponding physical responses. This process involves frequent data interaction, and thus we developed custom MATLAB code with the continual interaction between

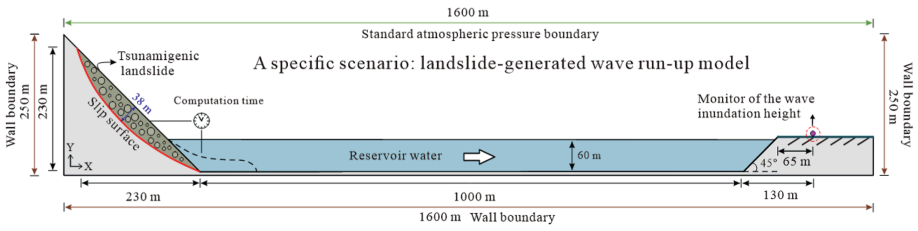

Fig. 4. Overview of simulation setup following a specific scenario: landslide-generated wave run-up. One point (pink dot) records the wave run-up height.

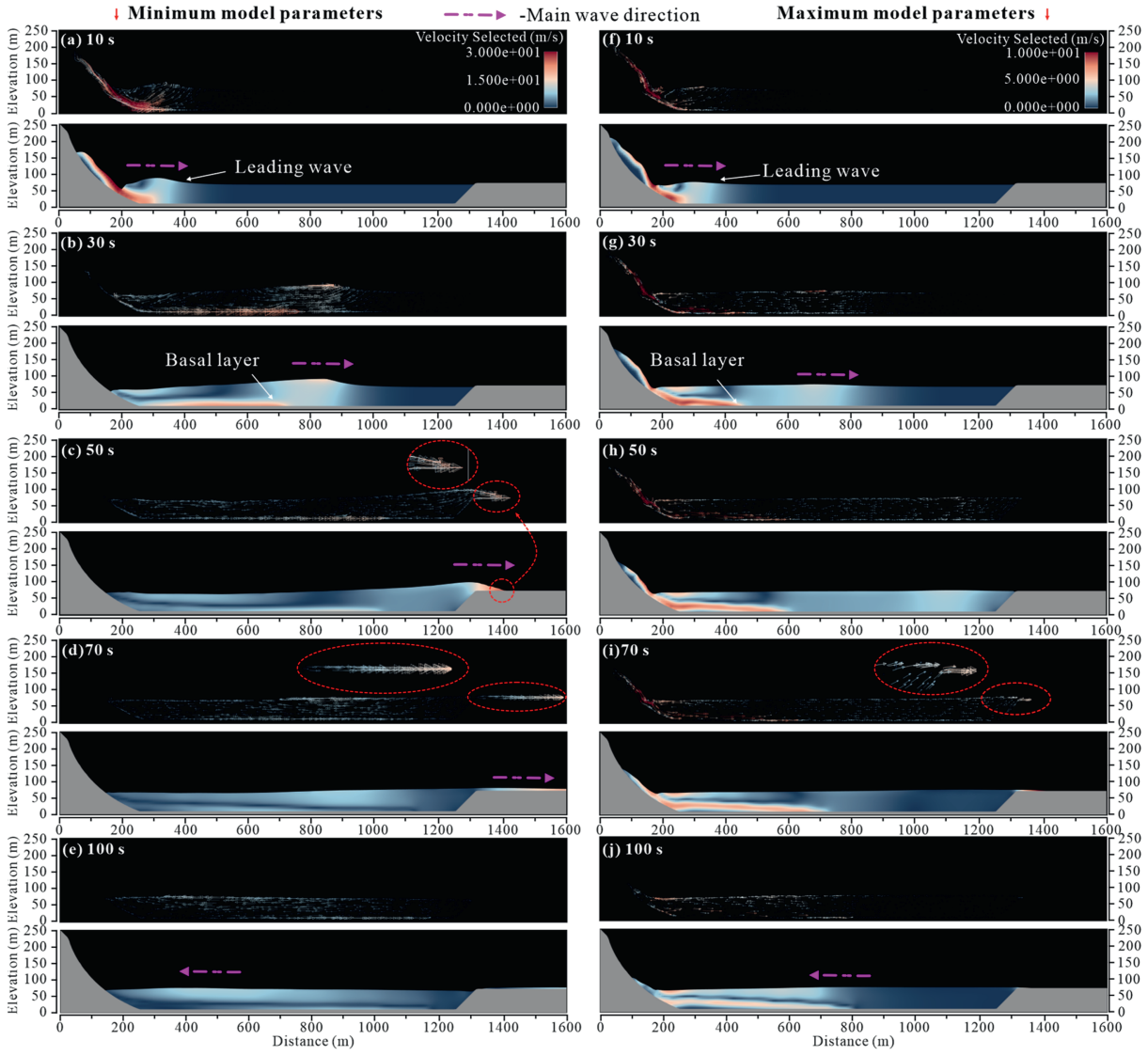

Fig. 5. In low strata of the panel, snapshots of the evolution in time (t = 10, 30, 50, 70, and 100 s from panels (a) to (e) and (f) to (j), respectively) of interaction between the landslide flow with threshold model parameters and the water body (left column with minimum and right column with maximum): (a, f) Landslide impact and wave generation, (b, g, h) Propagation of wave, (c, d, i) Wave run-up and inundation, and (e, j) Reflection of the wave. In the upper strata of the panel, the corresponding vector direction of the fluid (landslide and waves).

Table 1
Values of fluid parameters in previous literature.

Source	d (m)	ρ_g (kN/m^3)
Long et al. (2024)	0.01	2650
Sabeti and Heidarzadeh (2022)	0.01	2600
Chen et al. (2023)	0.1	2260
Franco et al. (2021)	1	2150–2650
Kim et al. (2020)	0.5	2600
Huang et al. (2017)	0.4	2640
Shi et al. (2024)	0.05	2600
Wu et al. (2024)		2200–2300

MATLAB and Flow3D (Li et al., 2024a). The stopping criterion $\varepsilon_{\mathrm{NRMSE}} = 0.02$ defined in Eq. (9) must be met for five consecutive iterations. Fig. 6 presents the evolution of root mean square errors (RMSEs) for both the TEAD and $\mathrm{RE_v}$ models throughout the refinement process, which requires 284 deterministic analyses. Throughout the entire evolution process, the RMSEs of $\mathrm{RE_v}$

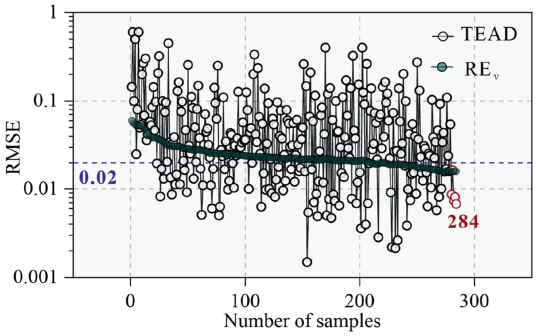

Fig. 6. Evolution of RMSEs of TEAD (black dots) and $\mathrm{RE_v}$ (green dots) as the sample size. Note that the red dots represent five consecutive points that meet the stopping criterion $\varepsilon_{\mathrm{NRMSE}} \leq 0.02$.

consistently decreased, thereby enhancing the global accuracy of the Kriging model. Upon satisfying the convergence criterion, the

RMSE for RE_v falls below the threshold of 0.02. Although the TEAD exhibits greater fluctuations compared to RE_v, ensuring that Eq. (9) is satisfied over five consecutive iterations can effectively guarantee the overall accuracy of the Kriging model. It should be noted that computational cost per iteration increases as the sample size grows over the adaptive sampling procedure. Using a MATLAB environment equipped with an Intel Core i7-12700F CPU (2.10 GHz) and 32 GB RAM, each iteration in this study required less than 30 s, which is negligible compared to the time-intensive deterministic fluid dynamics simulations. The total computation time of AK-PDEM (7.8 h) is very time-saving compared to the MCS (53 d).

In this section, a comparison of Markov Chain Monte Carlo (MCMC) with 50,000 deterministic analyses is used to demonstrate the effectiveness of AK-PDEM. One thousand representative points are generated using the GF-discrepancy method, and their probabilities are assigned by integrating the joint PDF over Voronoi cells (Zhou and Li, 2022). The constructed AK model is employed to evaluate responses of representative points, and the PDEM is then used to provide the PDF of the maximum run-up height (Fig. 7a). It can be clearly observed that the AK-PDEM can align with the results of MCMC, with a slight deviation at the maximum probability, which is ascribed to the nonlinear problem of LIWR. In this specific scenario, we focus on the wave-inundation threat for the low/mid-rise building (i.e. buildings with one to six stories), where each story maintains a 3.3 m height with a 3.3 m and 4.0 m ground story (GB50010-2010, 2010). Based on this, performance functions in Eq. (15) are established to develop the exceedance probability curves. The obtained exceedance probability curve still meets the accuracy requirements with a maximum standard deviation of 1.7 % (Fig. 7b). The potential threat range is classified into five zones (very high, high, medium, low, and very low) in light of the exceedance probability zoning proposed by Lacasse and Nadim (2012). Zones with exceedance probabilities above 50 % are considered most susceptible to wave impacts. It can be observed that one- and two-story buildings fall in the very high-risk zone and the three-story building with a 3.3 m ground story is also the high-risk zone (Fig. 8).

4.2. Example II: landslide-generated wave run-up with water level variation

4.2.1. Background of example II

For reservoir landslides, fluctuations in reservoir water level represent a primary failure factor, and thus we construct a specific actual-scenario model: Gongjiafang landslide with water level variation. The Gongjiafang landslide is located on the north bank of the Yangtze River in Wu Gorge (Huang et al., 2012; Du et al., 2020). A volume of 38×10^4 m^3 landslide in the Three Gorges Reservoir on November 23, 2008, led to a 12 m wave run-up on the opposite bank and losses of ~0.73 million US dollars (Fig. 9). A 2D numerical model with 50 m thickness has an orthogonal grid size of 5 m and a computational time of 100 s considering the balance between computation cost and accuracy (Fig. 10). Additionally, the top and bottom of the *X*-direction and the bottom of the *Y*-direction are defined as wall boundaries (Fig. 10). The standard atmospheric pressure boundary is set at the top of the *Y*-direction. The symmetric wave absorbers are defined along the thickness, with the damping coefficient gradually increasing from zero to four, which is similar to Example I. The sliding mass starts from rest and impacts the water, with a gravitational acceleration of 9.81 m/s^2.

4.2.2. Random variables and deterministic analysis

The d is assumed to be normally distributed with a mean of 0.225 m and standard deviation of 0.044 m based on on-site measurements with 0.05–0.40 m (Bolin et al., 2014). The ρ_g is intrinsically linked to material integrity, resulting in the challenge to define a certain value. Given that the study area primarily consists of limestone and marlstone, ρ_g is assumed to follow a normal distribution in 2300–2700 kg/m^3, with a mean of 2500 kg/m^3 and a standard deviation of 66.7 kg/m^3. This assumption is based on practical experience (Bell, 2007) and laboratory tests (Gu and Huang, 2016) in the study region. The surface roughness parameter R_r follows a uniform distribution of 1–4 m (Franco et al., 2021). In addition, different water levels might cause different run-up heights (Chen et al., 2024), and thus the quantification of water level uncertainty is meaningful for risk assessment. In this example, the reservoir water level includes two interesting problems: (1) Because it is determined based on measurements at the dam front, an inherent deviation develops between these recorded levels and the actual water surface in the study area; (2) From the perspective of prediction, the reservoir water level is uncertain because the landslide failure occurs in the trial impoundment phase of the Three Gorges Reservoir. When conducting reliability analysis, the effectiveness of the parameter range influences the prediction performance (Li et al., 2024a). Predicting in years obviously increases the uncertainty of the parameters, and thus we herein conduct prediction on a monthly basis. To this end, the water levels in October and December are used to predict the tsunami run-up generated by the Gongjiafang landslide. In terms of the original impoundment plan, the reservoir water level was raised from 170 m in October to 175 m in December (Yin et al., 2016; Tang et al., 2019), and the landslide occurred in November 2008. Therefore, the water level is assumed to be uniformly distributed within 170–175 m (Fig. 10).

Two deterministic analyses with model parameter thresholds (Minimum: $d = 0.05$ m, $\rho_g = 2300$ kg/m^3, $R_r = 1$ m; Maximum: $d = 0.4$ m, $\rho_g = 2700$ kg/m^3, $R_r = 4$ m) and 172.8 m water level

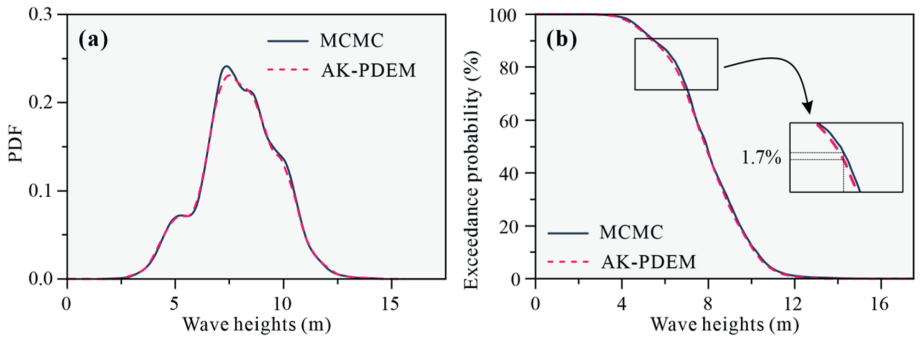

Fig. 7. PDFs and exceedance probability curves of wave heights using MCMC and AK-PDEM.

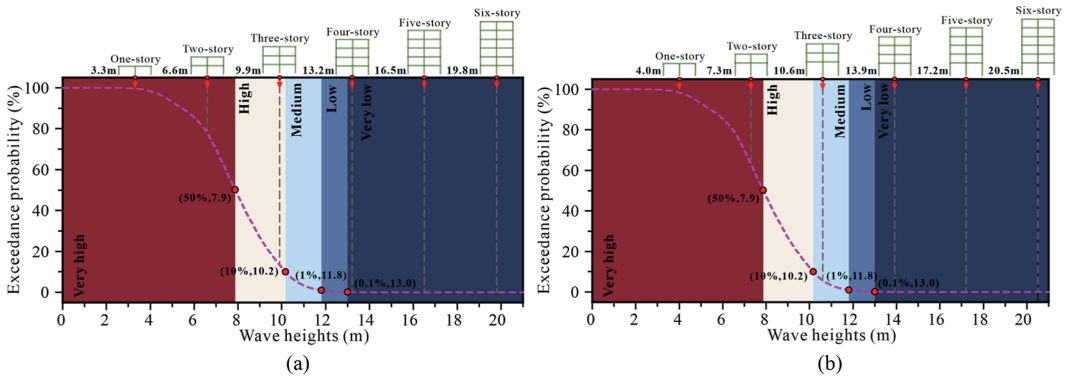

Fig. 8. The hazard zoning of LIWR for low/mid-rise buildings with (a) 3.3 m and (b) 4.0 m ground story.

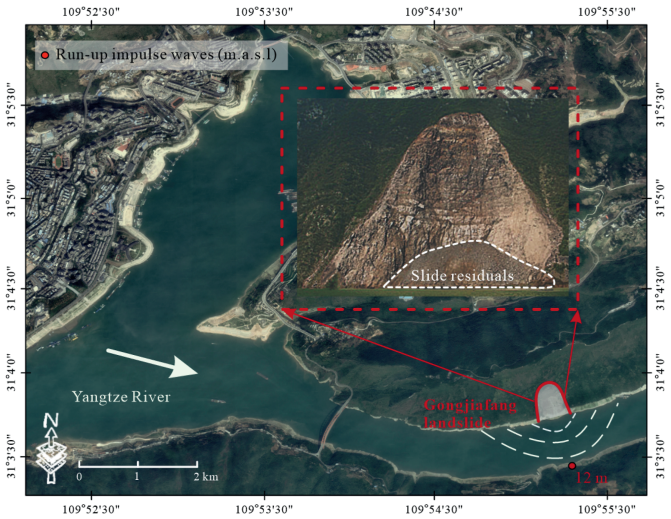

Fig. 9. The aerial photomosaic of Gongjiafang landslide occurring on November 23, 2008. The red dot is the recorded run-up height.

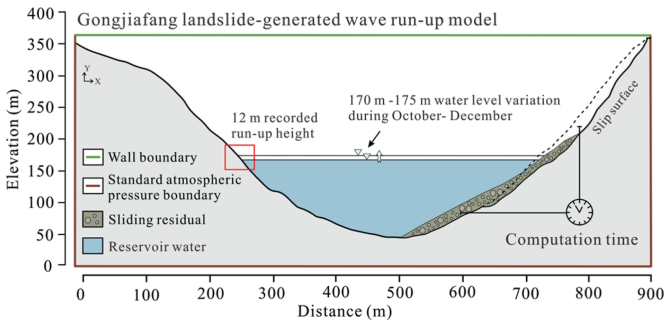

Fig. 10. Overview of simulation setup following an actual scenario: Gongjiagfang landslide-generated wave run-up. Note that the Gongjiagfang landslide with a 12 m run-up height occurs in November during the reservoir water storage period. According to the water storage plan (Tang et al., 2019; Yin et al., 2016), the 170 m and 175 m are water level elevations in October and December, respectively. The water level elevation is assumed to be uniformly distributed within 170–175 m during October and December due to impoundment.

(landslide instability) are conducted in Fig. 11. It can be observed that variations in the volume of the landslide entering the reservoir result in waves of different magnitudes. In terms of the minimum model parameters, the entire landslide mass slides into the reservoirs; conversely, the slide residuals accumulate at the slip surface for the maximum model parameters. This phenomenon underscores the necessity of quantifying parameter uncertainty in prediction.

4.2.3. Reliability assessment of landslide-induced tsunami

Similar to the Example I process, the AK model $\widehat{M}(\boldsymbol{\theta})$ with acceptable performance is constructed to approximate wave run-up heights from numerical simulation, which maps the relationship between four parameters (d, ρ_g, R_r, and water level) and simulations. Once the run-up heights of representative points are obtained via $\widehat{M}(\boldsymbol{\theta})$, the PDEM is employed to estimate the PDF. Based on the construction of the performance function and hazard zoning standard, the exceedance probability curve and hazard zones are presented accordingly.

For the AK model construction, 40 initial samples are generated, and a stopping condition $\varepsilon_{\text{NRMSE}} = 0.02$ is set for five consecutive iterations. For performing PDEM, 1000 representative points are generated via GF-discrepancy, which is used for the candidate sample pool. Fig. 12 presents the evolution of RMSEs in the AK model updating, and the sample size is 315 when it meets the stopping condition, which means the AK model only needs 315 samples to approximate 1000 responses. Using PDEM and these responses, the PDF of the wave run-up height is described in Fig. 13a, and then the exceedance probability curves are presented in Fig. 13b based on Eq. (16). Due to no element at risk in the opposite bank, we construct a performance function according to the observed wave run-up height (12 m), thereby obtaining the exceedance probability of 43 %. This result indicates the high risk of LIWR inundating this location (Fig. 14). It can be observed that the value (11.59 m) with a 50 % exceedance probability is close to the observation (12 m), which emphasizes the rationality of the theoretical statement in Example I. In summary, the AK-PDEM approach effectively identifies the predominant wave-inundation zones, quantifying involved parameter uncertainty, and optimizing the predictive performance of numerical simulations.

5. Discussion

5.1. The importance of considering parameter uncertainty

Because landslide-induced waves exhibit complex rheological behavior, landslide parameters are considered parameter ranges rather than fixed values. Employing only mean or specific parameter values typically results in poor predictive performance. For the numerical method in this study, the three principal model parameters are considered as random variables to input in the numerical simulation. Fig. 15 presents the results obtained by

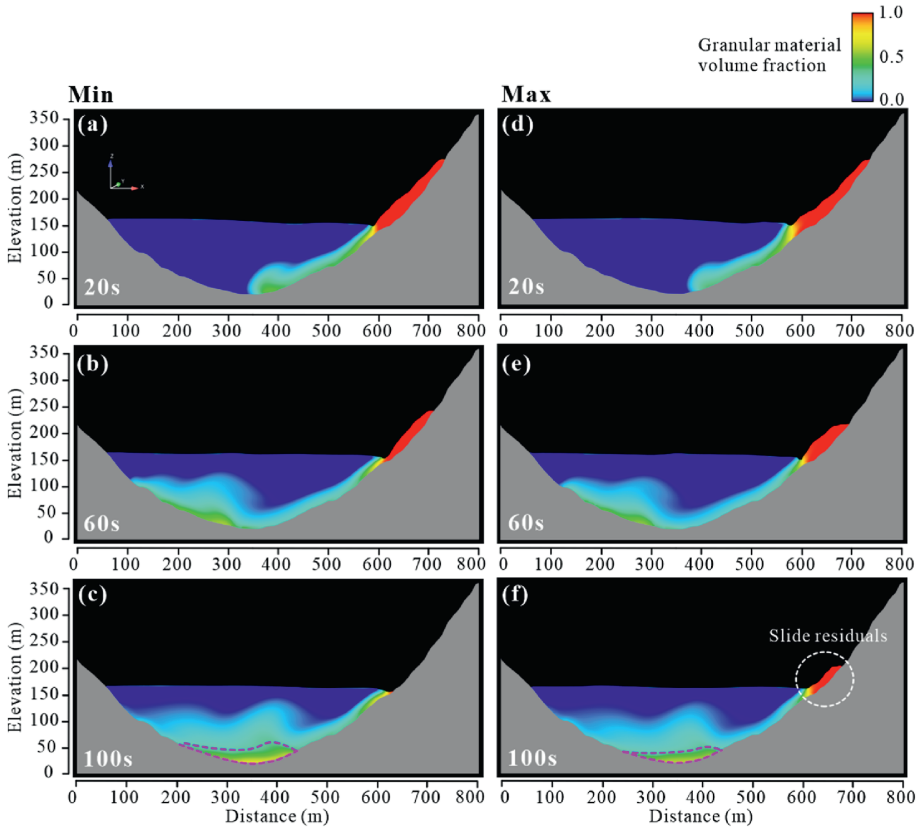

Fig. 11. A comparison between numerical simulations with (a–c) minimum and (d–f) maximum model parameters for the Gongjiafang landslide. Note that the minimum parameters: $d = 0.05$ m, $\rho_g = 2300$ kg/m^3, $R_r = 1$ m; maximum parameters: $d = 0.4$ m, $\rho_g = 2700$ kg/m^3, $R_r = 4$ m.

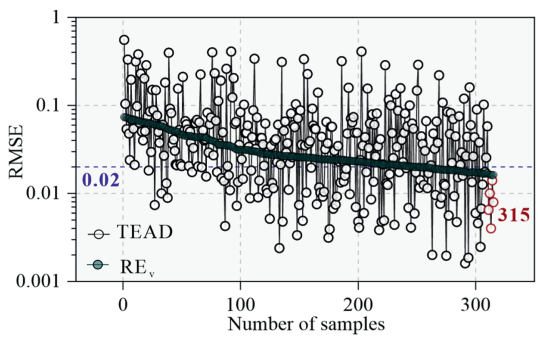

Fig. 12. Evolution of RMSEs of TEAD (black dots) and RE$_v$ (green dots) as the sample size. Note that the red dots represent five consecutive points that meet the stopping criterion $\epsilon_{NRMSE} \leq 0.02$.

varying one parameter at a time while holding the other parameters at their mean values. It can be observed that the uncertainties in model parameters cause the 11.02 m maximum wave height difference. At the building location of interest, the maximum difference is 7.59 m, which is equivalent to the height of a three-story building. These results underscore the importance of considering parameter uncertainty.

5.2. Advantages and remarks

This study proposes an efficient method to solve the challenge of model parameter uncertainty, focusing on reliability analysis and hazard zoning for LIWR. The proposed method offers a solid foundation for practical hazard prevention and mitigation efforts. Notably, it not only enables precise quantification of model

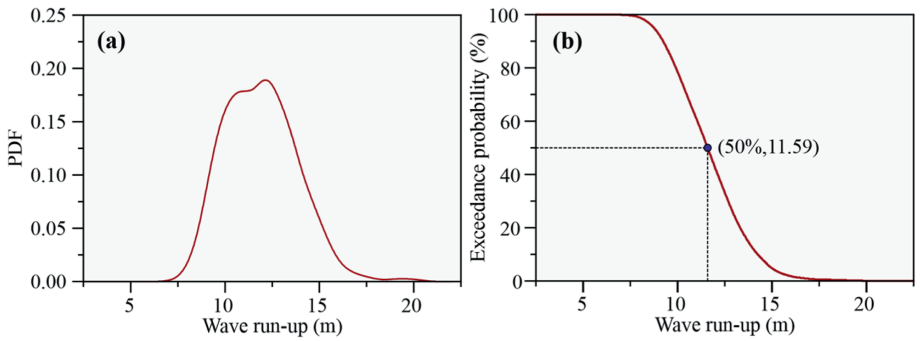

Fig. 13. (a) PDFs and (b) exceedance probability curves of wave run-up heights using AK-PDEM.

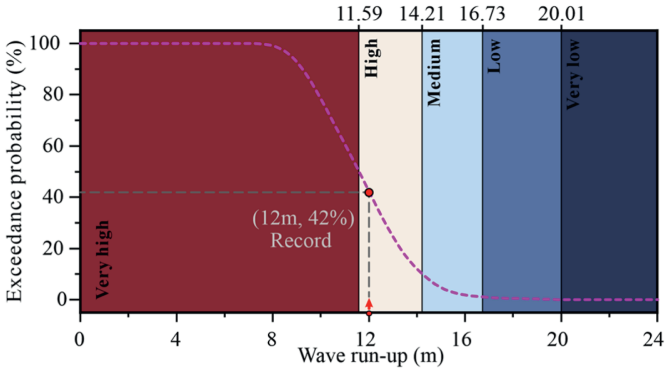

Fig. 14. The hazard zoning of LIWR for Gongjiafang landslide. Note that the red dot represents the real wave run-up height.

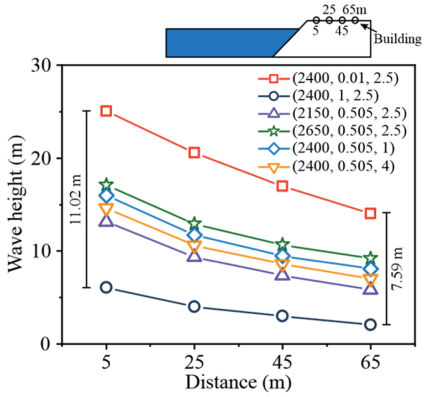

Fig. 15. Sensitivity analysis of model parameters. Note that in the legend: density ρ_g [2150–2650] kg/m^3, grain diameter d [0.01–1] m, and surface roughness R_r [1–4] m, respectively; 2400 kg/m^3, 0.505 m, and 2.5 m are the mean values of the three parameters.

parameters but also accounts for water level uncertainty. The procedure holds significant implications for predicting LIWR during water level fluctuation phases. Compared to MCMC with 50,000 samples and PDEM with 1000 samples, the proposed method achieves substantial computational efficiency, requiring only 284 deterministic analyses. Despite an increase in computational cost per iteration with larger sample sizes, each iteration in our MATLAB environment—running on an Intel Core i7-12700F CPU (2.10 GHz, 32 GB RAM)—completes within 30 s; this duration is negligible compared to the time required for deterministic fluid dynamics analyses.

In the landslide-wave probabilistic analysis, it should be underscored that the AK-PDEM method is not limited to run-up height, which can efficiently evaluate PDFs of different physical responses, such as depth-averaged velocity. This advantage will promote evaluating wave impact, enabling quantitative analysis of building vulnerability. Nonetheless, several limitations remain for future research:

(1) The current method focuses on the implementation of subaerial landslide-induced wave hazards, which are also suitable for submarine landslides. However, submarine landslide parameters are often more difficult to obtain. The proposed AK method can combine the Bayesian back analysis method to solve this problem.
(2) This study focuses on the model of the specific scenario and emphasizes the important role of the leading wave. We focus on the threat posed by the maximum wave height, solving the problem through 0–1 virtual time. The performance of AK-PDEM might be degraded for LIWR in a narrow basin with the multimodal distribution of responses due to wave overlap and reflection playing a predominant role. It is worth further investigating the time-evolution multimodal problem in future work.
(3) This method possesses good adaptability and can be combined with other numerical simulation techniques to quantify uncertainty in relevant parameters; however, the primary computational cost of this procedure depends on deterministic analysis (i.e. fluid dynamics simulation). Excellent computer equipment and efficient numerical methods are crucial for improving prediction efficiency in future work.

6. Conclusions

In this study, an AK-PDEM method, which incorporated the AK model and PDEM, was proposed for assessing LIWR hazards. Two examples were utilized to demonstrate the effectiveness of the proposed method and to highlight the influence of parameter uncertainties. The findings are summarized as follows:

(1) Compared with MCS-based deterministic analysis, the AK-PDEM method not only could effectively quantify the parameter uncertainties in the specific scenario: LIWR, but also achieved satisfactory accuracy, which was essential for rapid hazard zoning.
(2) For the evolution process of the specific scenario in this study, the landslide-triggered wave is a high-amplitude, solitary-like leading wave that displays a unimodal distribution evolving over time and is closely associated with the maximum run-up height.
(3) A probabilistic criterion was introduced to classify the hazard zone based on the probability that the maximum run-up height exceeds the element at risk, optimizing the traditional deterministic hazard evaluation for LIWR and providing a more intuitive recognition for reservoir managers.

CRediT authorship contribution statement

Ningjie Li: Methodology, Formal analysis, Writing – original draft, Funding acquisition, Conceptualization, Investigation, Data curation. **Xinli Hu:** Validation, Resources, Visualization, Software, Writing – review & editing, Supervision, Project administration. **Jian Wang:** Funding acquisition, Investigation, Conceptualization, Methodology, Formal analysis. **Junxiang Huang:** Supervision, Conceptualization, Validation, Methodology, Project administration. **Hongchao Zheng:** Supervision, Validation, Visualization, Resources. **Wei Li:** Project administration, Conceptualization, Data curation, Formal analysis.

Declaration of competing interest

The authors declare that they have no known competing financial interests or personal relationships that could have appeared to influence the work reported in this paper.

Acknowledgments

This study is supported by the Major International (Regional) Joint Research Project of the NSFC (Grant No. 42020104006) and

the National Major Scientific Instruments and Equipment Development Projects of China (Grant No. 41827808). The authors would express their sincere appreciation to anonymous reviewers and editors for their valuable comments and suggestions.

Appendix A. Supplementary data

Supplementary data to this article can be found online at https://doi.org/10.1016/j.jrmge.2025.06.018.

References

Alhamid, A.K., Akiyama, M., Ishibashi, H., Aoki, K., Koshimura, S., Frangopol, D.M., 2022. Framework for probabilistic tsunami hazard assessment considering the effects of sea-level rise due to climate change. Struct. Saf. 94, 102152.

Behrens, J., Løvholt, F., Jalayer, F., et al., 2021. Probabilistic tsunami hazard and risk analysis: a review of research gaps. Front. Earth Sci. 9, 628772.

Bell, F.G., 2007. Engineering Geology. Butterworth-Heinemann, Netherlands.

Bellotti, G., Cecioni, C., De Girolamo, P., 2008. Simulation of small-amplitude frequency-dispersive transient waves by means of the mild-slope equation. Coast. Eng. 55, 447–458.

Bolin, H., Yueping, Y., Xiaoting, C., Guangning, L., Sichang, W., Zhibing, J., 2014. Experimental modeling of tsunamis generated by subaerial landslides: two case studies of the three gorges reservoir, China. Environ. Earth Sci. 71, 3813–3825.

Cecioni, C., Romano, A., Bellotti, G., Risio, M., de Girolamo, P., 2011. Real-time inversion of tsunamis generated by landslides. Nat. Hazard Earth Sys. 11, 2511–2520.

Cecioni, C., Iorio, V., Bellotti, G., Grilli, S.T., 2023. Probabilistic landslide tsunami modeling of the 2018 palu Bay event. Coast. Eng. 183, 104332.

Chen, J.-B., Li, J., 2007. The extreme value distribution and dynamic reliability analysis of nonlinear structures with uncertain parameters. Struct. Saf. 29, 77–93.

Chen, J., Li, J., 2008. Strategy for selecting representative points via tangent spheres in the probability density evolution method. Numer. Methods Eng 74, 1988–2014.

Chen, J., Yang, J., Li, J., 2016. A GF-discrepancy for point selection in stochastic seismic response analysis of structures with uncertain parameters. Struct. Saf. 59, 20–31.

Chen, S., Shi, A., Xu, W., Yan, L., Wang, H., Tian, L., Xie, W.-C., 2023. Numerical investigation of landslide-induced waves: a case study of wangjiashan landslide in baihetan reservoir, China. Bull. Eng. Geol. Environ. 82, 110.

Chen, S., Xu, W., Zhang, G., Wang, R., Yan, L., Zhang, H., et al., 2024. Numerical simulation of potential impulse waves generated by the mogu rock landslide at varying water levels in the lianghekou reservoir, China. Landslides 21, 2289–2305.

Di Risio, M., Bellotti, G., Panizzo, A., De Girolamo, P., 2009. Three-dimensional experiments on landslide generated waves at a sloping Coast. Coast. Eng. 56, 659–671.

Du, J., Yin, K., Glade, T., Woldai, T., Chai, B., Xiao, L., Wang, Y., 2020. Probabilistic hazard analysis of impulse waves generated by multiple subaerial landslides and its application to Wu gorge in three gorges reservoir, China. Eng. Geol. 276, 105773.

Enet, F., Grilli, S.T., Watts, P., 2003. Laboratory experiments for tsunamis generated by underwater landslides: comparison with numerical modeling. In: The 13th International Offshore and Polar Engineering Conference. Honolulu, Hawaii, USA.

Engelund, S., Rackwitz, R., 1993. A benchmark study on importance sampling techniques in structural reliability. Struct. Saf. 12, 255–276.

Flow Science Inc, 2020. FLOW-3D® Solver, Version 12.2. Flow Science. Inc., Santa Fe, NM.

Franco, A., Moernaut, J., Schneider-Muntau, B., Strasser, M., Gems, B., 2021. Triggers and consequences of landslide-induced impulse waves – 3D dynamic reconstruction of the taan fiord 2015 tsunami event. Eng. Geol. 294, 106384.

Fritz, H.M., Hager, W.H., Minor, H.-E., 2004. Near field characteristics of landslide generated impulse waves. J. Waterw. Port, Coast. Ocean Eng. 130, 287–302.

GB50010-2010, 2010. Code for Design of Concrete Structures. China Architecture & Building Press, Beijing.

Gibbons, S.J., Lorito, S., Macías, J., Løvholt, F., et al., 2020. Probabilistic tsunami hazard analysis: high performance computing for massive scale inundation simulations. Front. Earth Sci. 8, 591549.

Grilli, S., Taylor, O.-D., Baxter, C., Maretzki, S., 2009. A probabilistic approach for determining submarine landslide tsunami hazard along the upper east Coast of the United States. Mar. Geol. 264, 74–97.

Grilli, S.T., Shelby, M., Kimmoun, O., Dupont, G., Nicolsky, D., Ma, G., Kirby, J.T., Shi, F., 2017. Modeling coastal tsunami hazard from submarine mass failures: effect of slide rheology, experimental validation, and case studies off the US east Coast. Nat. Hazards 86, 353–391.

Gu, D., Huang, D., 2016. A complex rock topple-rock slide failure of an anaclinal rock slope in the Wu gorge, yangtze river, China. Eng. Geol. 208, 165–180.

Hirt, C.W., 2010. A continuum model for high concentration granular media: illustrated by application to sand core blowing. Flow Science Report 10–TN88.

Huang, B., Dong, X., 2024. Experimental study on energy reduction and wave descent of typical landslide-induced impulse waves. Chin. J. Rock Mech. Eng. 43, 1397–1405 (in Chinese).

Huang, B., Hu, L., 2023. Scaled experimental study on impulse wave generated by a typical semi-submerged landslide with a low froude number in reservoir areas—Taking wangjiashan landslide as an example. J. Rock Mech. Geotech. Eng. 42, 1899–1909 (in Chinese).

Huang, B., Yin, Y., Liu, G., Wang, S., Chen, X., Huo, Z., 2012. Analysis of waves generated by gongjiafang landslide in Wu gorge, three gorges reservoir, on November 23, 2008. Landslides 9, 395–405.

Huang, B., Yin, Y., Wang, S., Tan, J., Liu, G., 2017. Analysis of the tangjiaxi landslide-generated waves in the zhexi reservoir, China, by a granular flow coupling model. Nat. Hazards Earth Syst. Sci. 17, 657–670.

Iorio, V., Bellotti, G., Cecioni, C., Grilli, S.T., 2021. A numerical model for the efficient simulation of multiple landslide-induced tsunami scenarios. Ocean Model. 168, 101899.

Javdanian, H., Pradhan, B., 2019. Assessment of earthquake-induced slope deformation of Earth dams using soft computing techniques. Landslides 16, 91–103.

Jiang, S.-H., Jie, H.-H., Xie, J., Huang, J., Zhou, C.-B., 2024. Probabilistic back-analysis of rainfall-induced landslides for slope reliability prediction with multi-source information. J. Rock Mech. Geotech. Eng. 16, 3575–3594.

Kamphuis, J.W., Bowering, R.J., 1970. Impulse waves generated by landslides. In: Coastal Engineering 1970.

Kim, J., Løvholt, F., Issler, D., Forsberg, C.F., 2019. Landslide material control on tsunami genesis—the storegga slide and tsunami (8,100 years BP). J. Geophys. Res.-Oceans 124, 3607–3627.

Kim, G.-B., Cheng, W., Sunny, R.C., Horrillo, J.J., McFall, B.C., et al., 2020. Three dimensional landslide generated tsunamis: numerical and physical model comparisons. Landslides 17, 1145–1161.

Lacasse, S., Nadim, F., 2012. Learning to live with geohazards: from research to practice. In: Geo-Risk 2011: Risk Assessment and Management, pp. 64–116.

Latifah, A.L., Tofany, N., Alphalevy, M.R.J., 2024. Landslide-generated wave simulation using coupled multi-phase flow and boussinesq-type models. Ocean. Eng. 300, 117461.

Li, S.-H., Luo, X.-H., Wu, L.-Z., 2021. A new method for calculating failure probability of landslide based on ANN and a convex set model. Landslides 18, 2855–2867.

Li, N., Hu, X., Zheng, H., Wang, J., Jing, X., Li, W., 2024a. A novel back analysis framework for the probabilistic risk assessment of subaerial landslide-induced tsunami hazard. Eng. Geol. 343, 107801.

Li, Y., Hu, X., Zhang, H., Zheng, H., Xu, C., 2024b. Nonlinear burgers model for sliding zone soil subjected to cyclic seepage pressure and its applications to the deformation analysis of landslide. Acta Geotech 20, 743–763.

Liao, K., Wu, Y., Miao, F., 2024. System reliability analysis of reservoir landslides: insights from long-term reservoir operation. J. Earth Sci.-China 35, 1583–1593.

Liu, D., Gong, X., Hu, X., Wang, H., Zheng, W., Niu, L., 2024. Displacement field reconstruction in landslide physical modeling by using a terrain laser scanner – part 1: methodology, error analysis and validation. J. Rock Mech. Geotech. Eng. 16, 4066–4076.

Long, X.-Y., Hu, Y.-X., Gan, B.-R., Zhou, J.-W., 2024. Numerical simulation of the mass movement process of the 2018 sedongpu glacial debris flow by using the fluid-solid coupling method. J. Earth Sci.-China 35, 583–596.

Løvholt, F., Harbitz, C.B., Haugen, K.B., 2005. A parametric study of tsunamis generated by submarine slides in the ormen lange/storegga area off Western Norway. In: Ormen Lange–an Integrated Study for Safe Field Development in the Storegga Submarine Area.

Lynett, P., Liu, P.L.-F., 2005. A numerical study of the run-up generated by three-dimensional landslides. J. Geophys. Res. 110, 2004JC002443.

Ma, H., Wang, H., Shi, H., Xu, W., Hou, J., Wu, W., Xie, W.-C., 2024. Probabilistic landslide-generated impulse waves estimation in Mountain reservoirs, a case study. Bull. Eng. Geol. Environ. 83, 494.

Mo, S., Lu, D., Shi, X., Zhang, G., Ye, M., Wu, J., et al., 2017. A taylor expansion-based adaptive design strategy for global surrogate modeling with applications in groundwater modeling. Water Resour. Res. 53, 10802–10823.

Montagna, F., Bellotti, G., Di Risio, M., 2011. 3D numerical modeling of landslide-generated tsunamis around a conical island. Nat. Hazards 58, 591–608.

Mulligan, R.P., Franci, A., Celigueta, M.A., Take, W.A., 2020. Simulations of landslide wave generation and propagation using the particle finite element method. J. Geophys. Res.-Oceans 125, e2019JC015873.

Panizzo, A., De Girolamo, P., Di Risio, M., Maistri, A., Petaccia, A., 2005a. Great landslide events in Italian artificial reservoirs. Nat. Hazard Earth Sys. 5, 733–740.

Panizzo, A., De Girolamo, P., Petaccia, A., 2005b. Forecasting impulse waves generated by subaerial landslides. J. Geophys. Res. 110, C12025.

Pradlwarter, H.J., Schuëller, G.I., Koutsourelakis, P.S., Charmpis, D.C., 2007. Application of line sampling simulation method to reliability benchmark problems. Struct. Saf. 29, 208–221.

Ruffini, G., Heller, V., Briganti, R., 2019. Numerical modelling of landslide-tsunami propagation in a wide range of idealised water body geometries. Coast. Eng. 153, 103518.

Sabeti, R., Heidarzadeh, M., 2022. Numerical simulations of water waves generated by subaerial granular and solid-block landslides: validation, comparison, and predictive equations. Ocean. Eng. 266, 112853.

Shi, A., Lei, J., Tian, L., Lyu, C., Mao, P., Xu, W., 2024. Benchmarking physical model

experiments with numerical simulations for the wangjiashan landslide-induced surge waves in the baihetan reservoir area. Water 16, 1930.
Si, P., Shi, H., Yu, X., 2018. A general numerical model for surface waves generated by granular material intruding into a water body. Coast. Eng. 142, 42–51.
Svennevig, K., Hicks, S.P., Forbriger, T., Lecocq, T., Widmer-Schnidrig, R., Mangeney, A., et al., 2024. A rockslide-generated tsunami in a Greenland fjord rang Earth for 9 days. Science 385, 1196–1205.
Tang, H., Wasowski, J., Juang, C.H., 2019. Geohazards in the three gorges reservoir area, China – lessons learned from decades of research. Eng. Geol. 261, 105267.
Tian, Z., Zhou, S., Lee, A., Zhao, Y., Gong, Q., 2024a. A Bayesian-based approach for inversion of Earth pressures on in-service underground structures. Acta Geotech 19, 1911–1928.
Tian, Z., Zhou, S., Lee, A., Shan, Y., Detmann, B., 2024b. How to identify Earth pressures on in-service tunnel linings: insights from Bayesian inversion to address non-uniqueness. Transp. Geotech. 48, 101344.
Tozato, K., Moriguchi, S., Takase, S., Otake, Y., Motley, M.R., Suppasri, A., et al., 2023. Optimal probabilistic placement of facilities using a surrogate model for 3D tsunami simulations. Nat. Hazards Earth Syst. Sci. 23, 1891–1909.
Walder, J.S., Watts, P., Sorensen, O.E., Janssen, K., 2003. Tsunamis generated by subaerial mass flows. J. Geophys. Res. Solid Earth 108.
Wang, L., Xiao, T., Liu, S., Zhang, W., Yang, B., Chen, L., 2023. Quantification of model uncertainty and variability for landslide displacement prediction based on monte carlo simulation. Gondwana Res. 123, 27–40.
Wang, X., Hu, X., Xu, C., Liu, C., Niu, L., Wang, J., 2024. Probabilistic stability analyses of the landslide-stabilizing piles system considering the spatial variability of geotechnical parameters. Bull. Eng. Geol. Environ. 83, 345.
Watts, P., Grilli, S.T., Kirby, J.T., Fryer, G.J., Tappin, D.R., 2003. Landslide tsunami case studies using a boussinesq model and a fully nonlinear tsunami generation model. Nat. Hazards Earth Syst. Sci. 3, 391–402.
Whittaker, C.N., Nokes, R.I., Lo, H.-Y., Liu, P.L.-F., Davidson, M.J., 2017. Physical and numerical modelling of tsunami generation by a moving obstacle at the bottom boundary. Environ. Fluid Mech. 17, 929–958.
Wiegel, R.L., 1955. Laboratory studies of gravity waves generated by the movement of a submerged body. Eos Transac. Am. Geophys. Union 36 (5), 759–774.
Wiegel, R.L., Noda, E.K., Kuba, E.M., Gee, D.M., Tornberg, G.F., 1970. Water waves generated by landslides in reservoirs. J. Waterw. Harb. Coast. Eng. Div. 96, 307–333.
Wu, C., Hong, L., Wang, L., Zhang, R., Pijush, S., Zhang, W., 2023. Prediction of wall deflection induced by braced excavation in spatially variable soils via convolutional neural network. Gondwana Res. 123, 184–197.
Wu, H., Zhong, Q., Deng, Z., Shan, Y., Zhao, K., 2024. Numerical investigation of the effect of landslide relative density on the impulse wave amplitude. Ocean. Eng. 309, 118563.
Yang, R., Huang, J., Griffiths, D.V., 2022. Optimal geotechnical site investigations for slope reliability assessment considering measurement errors. Eng. Geol. 297, 106497.
Yang, C., Liu, L.-L., Huang, F., Huang, L., Wang, X.-M., 2023. Machine learning-based landslide susceptibility assessment with optimized ratio of landslide to non-landslide samples. Gondwana Res. 123, 198–216.
Yang, Z., Yin, C., Li, X., Jiang, S., Li, D., 2024. Efficient slope reliability and sensitivity analysis using quantile-based first-order second-moment method. J. Rock Mech. Geotech. Eng. 16, 4192–4203.
Yavari-Ramshe, S., Ataie-Ashtiani, B., 2016. Numerical modeling of subaerial and submarine landslide-generated tsunami Waves—Recent advances and future challenges. Landslides 13, 1325–1368.
Yi, X., Feng, W., Wu, M., Ye, Z., Fang, Y., Wang, P., et al., 2022. The initial impoundment of the baihetan reservoir region (china) exacerbated the deformation of the wangjiashan landslide: characteristics and mechanism. Landslides 19, 1897–1912.
Yi, X., Feng, W., Li, B., Yin, B., Dong, X., Xin, C., Wu, M., 2023. Deformation characteristics, mechanisms, and potential impulse wave assessment of the wulipo landslide in the baihetan reservoir region, China. Landslides 20, 615–628.
Yin, Y., Huang, B., Wang, W., Wei, Y., Ma, X., Ma, F., et al., 2016. Reservoir-induced landslides and risk control in three gorges project on yangtze river, China. J. Rock Mech. Geotech. Eng. 8, 577–595.
Zhang, W., Wu, C., Tang, L., Gu, X., Wang, L., 2023. Efficient time-variant reliability analysis of bazimen landslide in the three gorges reservoir area using XGBoost and LightGBM algorithms. Gondwana Res. 123, 41–53.
Zhang, T., Wang, W., An, B., 2024. A massive lateral moraine collapse triggered the 2023 South Ihonak Lake outburst flood, Sikkim Himalayas. Landslides 22, 299–311.
Zhao, L., Mao, J., Bai, X., Liu, X., Li, T., 2016. Finite element simulation of impulse wave generated by landslides using a three-phase model and the conservative level set method. Landslides 13, 85–96.
Zhou, J., Li, J., 2022. An enhanced method for improving the accuracy of small failure probability of structures. Reliab. Eng. Syst. Saf. 228, 108784.

Dr. Xinli Hu is currently a Professor and PhD supervisor at Faculty of Engineering, China University of Geosciences, Wuhan, China. She is the member of International Association for Engineering Geology and the Environment (IAEG) and Engineering Geology Branch of China Geological Society. She has participated in a large number of research projects. Her research interests include (1) geohazard prevention and slope stability analysis; (2) deformation characteristics and failure mechanisms of reservoir landslides; (3) stabilizing pile-landslide interactions; and (4) physical and numerical modeling of landslide aspects.